Biomaterials Connect
ISSN: 3105-0387
2026, Article ID. 2026.0028, Cite as: https://doi.org/10.69709/BIOMATC.2026.166607

SCIFINITI PUBLISHING

Research Article

OPEN ACCESS

Age and Charge Effects in Cortical Bone: Raman Study of Phosphate Ions Stretching

Andrey Pavlychev[✉,1,*] **Xenia Brykalova**[✉,1] **Aleksei Konashuk**[✉,1] **Alexander A. Cherny**[✉,2] **Anatoliy Korneev**[✉,3]

[1] Department of Physics, St. Petersburg State University, Peterhof, Saint Petersburg 198504, Russia
[2] R.R. Vreden National Medical Research Center of Traumatology and Orthopedics, Saint Petersburg 195427, Russia
[3] Institute of Earth Sciences, St. Petersburg State University, Saint Petersburg 199034, Russia

Article History
Received: December 28, 2025 Accepted: May 14, 2026 Published: June 03, 2026

Abstract
A quantitative assessment of internal electrostatic fields in bone tissue was conducted within the framework of the "bone-battery" concept. The influence of these fields on atomic structure and dynamics may have been significantly underestimated. To test this hypothesis, Raman spectroscopy was applied to cortical bone samples from young and mature rats. Particular attention was given to the $\nu_1(PO_4^{3-})$ band at 960 cm^{-1} in the Raman spectra to investigate the coupling between P–O stretching vibrations and dipole polarization of PO_4^{3-} ions under electrostatic fields. The $\nu_1(PO_4^{3-})$-band was observed to split into bulk and interfacial components, which exhibited predominantly Gaussian and Lorentzian line shapes, respectively. The formation of these components is attributed to site- and age-dependent dipole polarization at the surfaces of bioapatite nanocrystals. Based on the experimental and theoretical results, the study suggests a possible memory effect during the mineralization of bioapatite nanocrystals, as well as quantum effects associated with low-dimensional quantization of valence states in hydrated nanolayers. The implications of these findings for nanoscale bone tissue engineering are also considered.

Keywords:
native bone; supercell; electrostatic fields; hydroxyapatite nanocrystal (HAPN); raman spectroscopy

1. Introduction

1.1. General Remarks

Increasing attention has been given to biomineralization mechanisms [1–3] because of their important role in the biosphere, including the lithosphere, hydrosphere, and atmosphere [4–6], as well as in living organisms under physiological and pathological conditions and in the development of biomimetic analogues [7–9]. Current microscopic understanding of biomineralization is primarily based on mineralogical and biomedical studies and relies mainly on X-ray diffraction and electron microscopy investigations (see, e.g., [10,11]). They show that the hard biological tissues form unique "organism-material" complexes [12–14], in which the dominant role is played by hexagonal calcium carbonate hydroxyapatite (HAP, $Ca_{10-x}(CO_3)_x(PO_4)_{6-x}(OH)_{2-x}$, $0 \leq x \leq 2$) with substantially variable stoichiometry that reflects the non-stationary conditions of their formation inside the voids of collagen fibers [15–19].

Variations in stoichiometry are governed by vacancies at Ca^{2+} and OH^- sites, as well as isomorphic substitutions at different crystallographic positions of HAP, with concentrations depending on the characteristics of the biogenic environment. Different authors have reported varying interpretations of these stoichiometric variations [13–15,18–23]. In particular, a recent study on age-related changes in bone [17] showed that deviations in stoichiometry can act as a source of charge heterogeneity within the mineral matrix. The interplay of size, stoichiometry, and charge effects may lead to novel structure–function relationships with distinctive mechanical and electrophysical

* **Corresponding Author:**
Andrey Pavlychev, Department of Physics, St. Petersburg State University, Peterhof, Saint Petersburg 198504, Russia, a.pavlychev@spbu.ru;
Tel.: +79119734999

2026, Vol. 3, Article ID. 2026.0028
https://doi.org/10.69709/BIOMATC.2026.166607

properties, thereby supporting further experimental and theoretical investigations into the atomic structure and dynamics of native bone.

1.2. The Bone-Battery Concept

A nanoscopic view of mineralized bone assembled from HAP nanocrystals (HAPNs) is presented in Figure 1. The HAPNs within a coplanar conglomerate are illustrated in the figure as shaded boxes separated by hydrated nanolayers. Because long-range order in HAPNs is disrupted, the electroneutrality condition that applies to individual unit cells in macro- and microcrystals may no longer hold for these nanostructures. Thus, owing to their small size and disrupted long-range order, these structures may behave as charged entities. To compensate for the charge distribution *Q(r)*, the electroneutrality condition in bone can be reformulated in a more general form [17].

$$\int_S \frac{d}{dr} Q(\boldsymbol{r}) d\boldsymbol{r} \equiv 0. \tag{1}$$

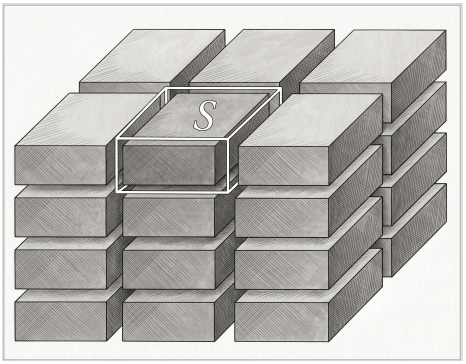

Figure 1: Schematic presentation of a planar conglomerate of HAPNs (shaded boxes) separated from each other by hydrated nanolayers. Supercell *S* is shown with white lines.

The integration region in Equation (1) is the supercell *S*, which is marked with white lines in Figure 1.

The supercell *S* includes both a HAPN and its adjacent hydrated nanolayers. Equation (1) suggests that the excess charge in a HAPN is compensated by opposite charges accumulated in the surrounding hydrated nanolayers. Charge distributions in mineralized bone are schematically illustrated in Figure 2.

Comparative analysis of temporal variations in electron binding energies, lattice constants, and calcium deficiency has predicted the accumulation of excess negative charge in HAPNs [17]. The built-in charge, *Q*, is reported to reach its maximum in newborn bone and decrease with age. The relationship

$$\Delta E_{core} = E^{HAP} - E^{bone} \approx -e\frac{Q}{4\pi\varepsilon_0}\left(\frac{1}{\varepsilon' < r' >} - \frac{1}{\varepsilon'' < r'' >}\right) > 0, \tag{2}$$

links the built-in charge Q with the spectral shift ΔE_{core} of core-electron BE and enables forecasting of charge alterations. The charge Q was estimated to be approximately 8 ± 3 e$^-$ in young bone and 3 ± 2 e$^-$ in mature bone [17]. In Equation (2) $< r' >$ and $< r'' >$ represent the average distances to vacant Ca^{2+} positions within a nanocrystal and to Ca^{2+} ions in the adjacent nanolayers, respectively, whereas, ε' and ε'' denote the dielectric constants of bioapatite and the intercrystallite environment.

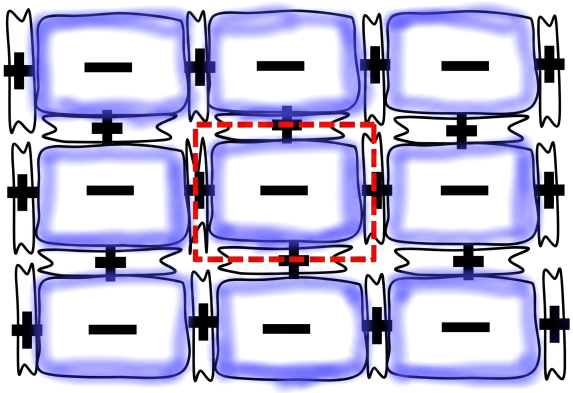

Figure 2: Schematic presentation of charge distribution in a coplanar HAPN conglomerate. Areas of strong changes in the electrostatic potential are highlighted in blue. The super (nano)cell is marked in red.

The nanoscale heterogeneity of charge distribution supports the interpretation of bone mineral as a battery-like system composed of many supercells, each formed by a negatively charged HAPN embedded within a positively charged hydrated medium.

Using the extracted charges and HAPN dimensions [17], the density of electrostatic energy associated with charge inhomogeneity was estimated to be $P > 10^6$ J/m^3 for young bone and $P < 10^5$ J/m^3 for mature bone. This estimation indicates the substantial decrease (more than 10 times) of the built-in energy $\mathcal{E}$ with age. These findings suggest that the effects of electrostatic fields in bone may have been substantially underestimated. Such fields may polarize atomic and molecular fragments, alter ionic dynamics, and potentially link aging processes with discharge-like phenomena in bone mineral.

1.3. Study Objectives

The "bone-battery" (BB) concept may open new perspectives for age- and patient-specific targeted drug delivery,

2026, Vol. 3, Article ID. 2026.0028
https://doi.org/10.69709/BIOMATC.2026.166607

the development of novel energy-related biomaterials, and advanced biomedical nanotechnologies aimed at promoting healthy aging.

The present study focuses on electrophysical phenomena associated with electrostatic fields induced by built-in charges and their impact on atomic dynamics in bone tissue. The primary objectives of this study are to characterize the strength and spatial distribution of electrostatic fields, quantitatively evaluate these fields, and clarify their role in aging-related phenomena.

Since the electrostatic field gradient is expected to be particularly strong at the interfaces between neighboring nanocrystals (see Figure 2), HAPN-associated atomic and molecular constituents can be approximately classified into two groups. The first group (*A*) comprises atomic and molecular constituents within the bulk, whereas the second group (*B*) includes atoms and molecular fragments at the interfaces, where electrostatic forces are expected to induce stronger distortions than in the bulk.

The nanocrystal-hydrated nanolayer interface is generally regarded as a more disrupted region [21]. However, electrostatic fields may promote dipole ordering of $[PO_4]^{3-}$, $[CO_3]^{2-}$, and $[OH]^{-}$ molecular ions, with a particularly pronounced effect in young bone. To test this hypothesis, the present analysis focuses on Raman scattering associated with P–O stretching vibrations. This choice is motivated by the presence of a narrow, intense $\nu_1[PO_4]^{3-}$ band at 960 cm^{-1} in Raman spectra, which is widely accepted as a key indicator of bone mineral content (see, e.g., [24–26]).

Considering the partitioning of PO_4^{3-} ions into bulk and interfacial populations, the $\nu_1(PO_4^{3-})$ Raman band in native bone may be expected to split into two components. One sub-band (*A*), associated with the bulk population, is expected to resemble the $\nu_1(PO_4^{3-})$ band in HAP, whereas the second sub-band (*B*), associated with interfacial regions, is expected to exhibit a red shift and noticeable distortion due to electrostatic field effects.

Against this background, the main objectives are (i) to detect and characterize the splitting of the $\nu_1[PO_4]^{3-}$ Raman band in young and mature bone and (ii) to compare the observed spectral behavior with that predicted by the bone-battery (BB) concept. Section 2 describes the methods used for sample preparation and Raman band analysis. Section 3 presents the evaluation of electrostatic fields in bone and reports the results of the experimental spectral analysis. Section 4 discusses Raman spectroscopic evidence supporting a relationship between built-in charges and age-related changes in bone tissue, consistent with predictions based on X-ray diffraction and X-ray photoelectron spectroscopy (XPS) [17,27].

2. Materials and Methods

2.1. Samples

Bone samples were prepared ex situ from the cortical layers of the mid-diaphysis of the femur, tibia, and humerus of white mongrel male rats, grouped as young (40–60 g; n = 8) and mature (250–280 g; n = 6). All animal-related procedures were conducted in accordance with applicable ethical requirements and reported following the ARRIVE guidelines. The study complied with applicable national regulations and international standards, including GOST R ISO 10993-2-2009 and relevant ISO 10993 standards related to animal welfare requirements. The study also followed GOST 33215-2014 and GOST 33216-2014, which define requirements for the maintenance and care of laboratory rodents and rabbits. The study protocol (10-10-2015) was approved by the Local Ethics Committee of the R.R. Vreden National Medical Research Centre of Traumatology and Orthopedics. All animals were maintained under standardized conditions in the vivarium of the National Medical Research Center of Traumatology and Orthopedics.

The cortical bone was thoroughly cleaned of soft tissue, rinsed with saline, blotted dry, and ground into a fine powder with particle sizes of approximately 1 mm. This sample preparation was not expected to affect the measured spectra, and no thermal treatment was applied to the bone samples. To compare bone mineral with reference hydroxyapatite, near-stoichiometric HAP crystals synthesized as described in [22,28] were used as reference compounds.

The structural parameters of the samples, determined by X-ray diffraction (XRD) [17,27], are summarized in Table 1. Table 1 presents the HAP lattice constants $a = b$ and c, mean linear size $\langle L \rangle$ of HAPNs, crystallinity degree *D*, mean nanolayer thickness $\langle d \rangle$, effective number of atoms *N* per HAPN, charge *Q* in young and mature bone, and the corresponding errors.

2.2. Raman Probing

Raman spectroscopy (see, e.g., [26]) enables phase identification in complex materials and detects subtle variations in light scattering, thereby providing insight into nanoscale effects. This method is a powerful tool for probing and mapping nanophases dispersed within matrices (see, e.g., [29,30]), surface nanophases [31], charge transport processes [32,33], film orientation [34], cluster size [35], configurational order [36], interfacial reactions [37], and mechanical loading effects [38]. This spectroscopic approach was used to investigate site-dependent

coupling between P–O stretching vibrations and dipole polarization of $[PO_4]^{3-}$ ions in young and mature bone.

Static disorder and dynamic dephasing represent two limiting mechanisms that give rise to Gaussian and Lorentzian broadening of Raman signals, respectively (see, e.g., [39]). The present study focuses on specific changes in Raman band shape. First, a two-component $v_1(PO_4{}^{3-})$ band structure was expected, enabling assessment of the differential effects of electric fields on bulk and interfacial components. Second, the agreement between the observed spectral behavior and predictions from the bone-battery model was evaluated. It was hypothesized that $[PO_4]^{3-}$ ions in the interfacial region undergo static disorder as well as polarization along the electric field lines. Accordingly, the Lorentzian character of sub-band *B* is expected to become more pronounced with increasing coherence of P–O stretching vibrations in the corresponding regions.

Table 1: Structural and charge parameters of the atomic–molecular architecture of young and mature bone samples. Structural parameters *a*, *c*, <*L*>, and <*d*> are given in Å, charge *Q* is in e^-, and *N* is the average number of atoms per HAPN.

Parameters	Young Bone	Mature Bone
a	9.413 ± 0.001	9.396 ± 0.001
c	6.849 ± 0.001	6.875 ± 0.001
<*L*>	35 ± 5	45 ± 5
<*d*>	12 ± 2	7.5 ± 2
D%	84 ± 4	96 ± 4
N	1800 ± 500	3800 ± 500
Q	8 ± 3	3 ± 2

This expectation supported the use of Voigt functions to approximate the experimental bands. This approach allows direct extraction of the Gaussian and Lorentzian widths, W_G and W_L, which were considered markers of static disorder and vibrational coherence of the $PO_4{}^{3-}$ units contributing to sub-bands *A* and *B*.

The fitting analysis showed that two Voigt functions provided an optimal model for the $v_1(PO_4{}^{3-})$ band in the bone specimens. To characterize the band shapes in young and mature bone, two Voigt functions are employed, with peak positions and Gaussian and Lorentzian widths treated as free parameters determined through best-fit optimization of the experimental data. This approach enabled a quantitative assessment of the applicability of the BB concept by comparing the extracted spectral widths with model-based predictions. In addition to spectral widths, variations in relative intensities and Raman shifts of the sub-bands in young and mature bone were analyzed to evaluate the proposed concept.

3. Results

3.1. Experimental

Raman measurements of bone samples and the reference hydroxyapatite crystal were performed over a wide spectral range of 300–4000 cm^{-1} and, in greater detail, within the narrow interval of 920–990 cm^{-1}. Measurements were carried out using both a Horiba Jobin-Yvon LabRAM HR800 Raman spectrometer (Science Park of Saint Petersburg State University; within the frameworks of projects 101-22060, 112-22072, 113-22068, 119-13853) and an Olympus BX41 microscope (40× objective) with a 532 nm excitation laser [40] (Prof. E. Rühl's laboratory, Freie University Berlin, within the framework of GRISC projects P-2017b-1 and P-2018b-12). Repeated Raman measurements of bone samples demonstrated good reproducibility. No sample charging or decomposition effects were observed.

The measured spectra of young and mature bone, together with the HAP reference, within the narrow spectral interval are shown in Figure 3. The smooth background, determined from wide-range Raman measurements, has been subtracted in the figure. The intense $v_1(PO_4{}^{3-})$ band in bone was substantially broadened and asymmetric compared with that in the HAP reference crystal. This broadening is expected because the crystalline structure of bone mineral is more disordered than that of HAP. However, the observed band asymmetry and its underlying origin require further investigation.

3.2. Assessment of Electrostatic Effects

To evaluate electrostatic fields, the concept of double electrical layers (DELs) was employed. The DEL effect in bone was previously reported by Wilson et al. [41]. Based

2026, Vol. 3, Article ID. 2026.0028
https://doi.org/10.69709/BIOMATC.2026.166607

on Nuclear Magnetic Resonance (NMR) spectral analysis, this effect was attributed to $[PO_4]^{3-}$ ions at the surfaces of HAPNs and their charge compensation by Ca^{2+} ions accumulated within hydrated nanolayers.

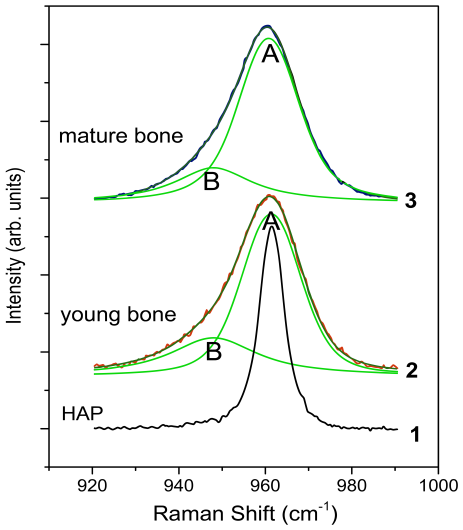

Figure 3: Experimental Raman spectra in the narrow interval 920–990 cm^{-1}. The measured $v_1[PO_4{}^{3-}]$-band in young and mature bone are shown as symbols, and the fitted bands are shown as thin lines. The extracted *A* and *B* components are shown as green lines. The $v_1[PO_4{}^{3-}]$ band in the HAP reference is also shown.

Within the BB concept, an alternative origin of DELs is proposed, where negatively charged layers arise mainly from the built-in charge Q rather than from broken phosphate bonds at the surface, Q. Considering the high mobility of hydroxide anions in HAP, it may be assumed that they are displaced from the bulk by intrinsic electrostatic repulsive forces and subsequently accumulate at the surfaces of HAPNs. Thus, the charge Q_{surf} attributed mainly to excess $[OH]^-$ rather than to $[PO_4]^{3-}$ groups. It is assumed that $Q_{surf} \geq Q$, and the contribution of phosphate ions is considered negligible due to surface relaxation effects in HAPNs.

In the interfacial region between two HAPNs, the electrostatic field can be approximately described as a superposition of two mirror-symmetric DELs. Figure 4 illustrates this model, where the left and right DELs correspond to the opposite ends of two neighboring HAPNs. Black and white triangles, as well as white and green hexagons, refer respectively to hydroxides, hydroxide vacancies, Ca^{2+} vacancies, and $Ca^{2+}(H_2O)_n$ clusters.

Next, the DELs are described as flat capacitors, (−||+) and (+||−), with negative plates formed by $[OH]^-$ anions at the surface and positive plates formed by Ca^{2+} cations compensating the total charge. This simple model makes it clear that hydrated nanolayers in bone represent potential wells $\varphi(x)$.

Assuming $L >> \frac{1}{2}d$, uniform distribution of Q_{surf}, linear dependence of electric field strength $\boldsymbol{F}$ in the capacitors, and neglecting edge effects in them, we derive that $\varphi(x)$ is a V-shaped potential well. In the interval $-\frac{1}{2}d \leq x \leq +\frac{1}{2}d$ it is

$$\varphi_V(x) = \frac{2\Delta\varphi}{d}|x|, \tag{3}$$

where, $\Delta\varphi$ is the potential difference:

$$\Delta\varphi \approx \frac{Q_{yz}}{C_{yz}}, \tag{4}$$

between the negative and positive charged plates. Q_{yz} represents the part of Q_{surf} associated with the yz plate (see Figure 4), and the capacitance C_{yz} is

$$C_{yz} = \frac{2\varepsilon''\varepsilon_0}{d} S_{yz}, \tag{5}$$

where S_{yz} is the surface area of the plate. The total capacity of a single HAPN is $C = \sum_{j,j\neq i} C_{ij}$. The directions of $\boldsymbol{F}$ are marked in Figure 4.

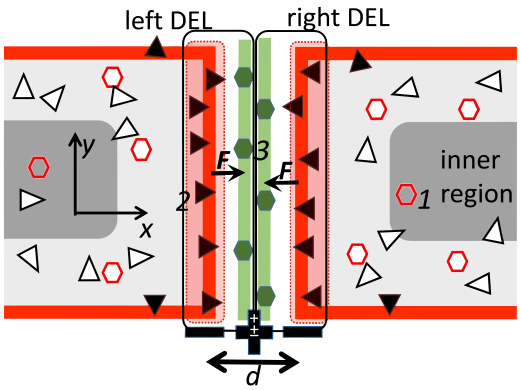

Figure 4: Schematic presentation of the contact region between two neighboring nanocrystals in bone; the solid red and green stripes refer to negatively and positively charged nanolayers of two DELs (see text). Black and white triangles refer to OH^- on the surface and OH^- vacancies in the bulk; white and green hexagons refer to Ca^{2+} vacancies and $Ca^{2+}(H_2O)_n$ clusters in hydrated layers, respectively. The inner region (see text) of HAPNs is darkened.

Using the sizes and charges in Table 1, neglecting age variations of ε' and ε'', considering that HAPNs in the bone samples are elongated along the *c* (||z) axis by about 5–6 times more than along the *x* and *y* axes and applying Equations (3) and (5), the potential difference and the electrostatic field strength are estimated as $\Delta\varphi^{young} \approx 140 \pm 50$ mV and $\boldsymbol{F}^{young} \approx 230 \pm 80$ kV/mm for young bone, respectively. In mature bone, the characteristics are reduced

2026, Vol. 3, Article ID. 2026.0028
https://doi.org/10.69709/BIOMATC.2026.166607

by more than an order of magnitude, reaching values of $\Delta\varphi^{mature} \approx 10$ mV and $\boldsymbol{F}^{mature} \approx 25$ kV/mm. Thus, it is inferred that, with aging, the potential well in the interfacial region becomes narrower and significantly shallower.

Figure 5 shows the potentials φ(r) for young and mature bone over a wider range. For comparison, it is assumed that $\varphi(r) \approx 0$ in the inner region of the HAPN (see Figures 4 and 5), because the Coulomb potentials created by Ca^{2+} and OH^- vacancies compensate each other due to the high mobility of hydroxide ions. Taking into account the charge distributions, the potential can be represented as:

$$\varphi(r) = \begin{cases} \frac{2\varphi}{d}|r| - V_0, & \text{for } -\frac{1}{2}d \; r \; +\frac{1}{2}d \\ e^{-\alpha r}, \text{ for } r \in (\pm\frac{1}{2}d, \pm\frac{1}{2}(b)) \end{cases}. \quad (6)$$

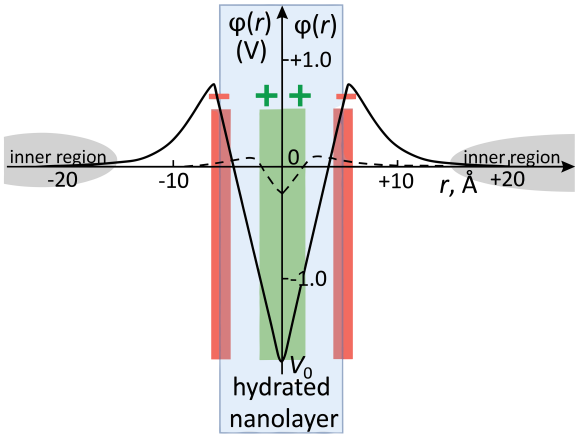

Figure 5: Schematic presentation of the potential $\varphi(r)$ in young (solid line) and mature bone (dashed line). Hydrated nanolayers are shown in light blue.

Inside the hydrated nanolayers, φ(r) represents a V-shaped potential well of depth V_0. Potential barriers are formed at the surfaces of HAPNs, and inside the HAPNs the potential φ(r) decreases exponentially. Here, b (=d + L) is the mean size of the supercell S and α determines the rate of decrease of potential. The model potential in Figure 5 is shown on a meV scale. In reality, it is smoothed because of the finite spatial extent of the charge distribution and thermal atomic motion.

The assessment of electrostatic fields supports the predicted trends in atomic dynamics in bone, as described in Section 1.3. In addition to static disorder, the interfacial region is expected to exhibit dipole alignment along the direction of the electrostatic forces. As a result, sub-band B is expected to show a more pronounced Lorentzian character than sub-band A in the Raman spectra of bone.

3.3. Data Analysis

To test these predictions, the measured $\nu_1(PO_4^{3-})$ bands in young and mature bone were analyzed in greater detail. The best-fit Voigt functions are shown as solid black lines in Figure 3. The extracted Raman shifts E_A and E_B, Lorentzian widths W_L, Gaussian widths W_G, full widths at half maximum of sub-bands A and B, and relative intensity $\frac{B}{A+B}$ are presented in Table 2. The spectroscopic parameters of the $\nu_1[PO_4]^{3-}$-band in HAP are also shown. The χ^2 values are also presented in Table 2. Since the spectral positions and Gaussian and Lorentzian widths were not fixed a priori, the extracted parameters were treated as independent characteristics of the sub-bands under study.

The spectroscopic parameters in Table 2 make evident the resemblance of the position of the intense high-frequency sub-band A with the $\nu_1[PO_4]^{3-}$-band in HAP crystal. The subband A exhibits a pronounced Gaussian profile ($W_G^A >> W_L^A$). As shown in Table 2, the Gaussian width W_G^A decreases by more than a factor of two with age, which is qualitatively consistent with the increased degree of crystallinity in mature bone compared with young bone. As for the Lorentzian width W_L^A varies weakly and is much smaller than W_G^A. Thus, the similarity of the Raman shift of sub-band A to the $\nu_1[PO_4^{3-}]$ band in crystalline hydroxyapatite (HAP), together with its Gaussian profile, allows sub-band A to be assigned to $[PO_4]^{3-}$ moieties in the bulk.

The sub-bands B in the spectra of both young and mature bone are shifted downward by 13.3 and 12.7 cm^{-1} compared to the $\nu_1[PO_4]^{3-}$-band in HAP. This pronounced shift indicates an association between sub-band B and interfacial PO_4^{3-} moieties.

Consistent with the proposed model, the extracted shapes of sub-bands A and B show clear differences. Sub-band B shows a predominantly Lorentzian character, with W_G^B much smaller than W_L^B, whereas sub-band A shows a predominantly Gaussian character in the Raman spectra of both young and mature bone. This difference may indicate strong static disorder in HAPNs, especially in young bone, as well as polarization of P–O dipoles in the contact region.

In addition to the distinctions in shape, Table 2 demonstrates (i) a minor but distinct downward displacement Δ_A of the sub-band A: E_A(mature) ≈ 960.7 cm^{-1} < E_A(young) ≈ 961.3 cm^{-1}, and (ii) a decrease in the contribution of the sub-band B to the total signal with age:

$$\frac{B}{A+B}(\text{mature}) \; < \; \frac{B}{A+B}(\text{young}). \quad (7)$$

2026, Vol. 3, Article ID. 2026.0028
https://doi.org/10.69709/BIOMATC.2026.166607

Table 2: Spectroscopic parameters of mineralized bone: Raman shifts $E_{A(B)}$, Lorentzian (W_L), and Gaussian (W_G) FWHM of the *A* and *B* components for young bone and mature bone. In HAP, only one Voigt function was used for fitting. The parameters are averaged over all bone samples.

Spectrosc. Parameters	HAP	Young Bone		Mature Bone	
		A	***B***	***A***	***B***
E in cm^{-1}	961.4 ± 0.2	961.3 ± 0.5	948 ± 0.5	960.7 ± 0.5	948 ± 0.5
W_L in cm^{-1}	4.7 ± 0.2	6 ± 1	13 ± 1	8.5 ± 1	21.5 ± 1
W_G in cm^{-1}	3.7 ± 0.2	24 ± 1	3 ± 1	11.5 ± 1	2 ± 1
Ratio $\frac{B}{A+B}$,	0	0.31 ± 0.05		0.24 ± 0.05	
Ratio $\frac{L}{G}$	1.3 ± 0.1	0.5 ± 0.1		1.3 ± 0.1	
Coeff χ^2	435	500		290	

4. Discussion

4.1. Electrostatic Effects

The assessment of electrostatic fields generated by embedded charges within the BB concept indicates that ion polarization at interfaces and within hydrated nanolayers should not be neglected. The Raman analysis of symmetric P–O vibrations in young and mature bone is consistent with this assessment.

However, it should be noted that the estimates of $\Delta\varphi$ and $\boldsymbol{F}$ were made using multiple approximations. Ca^{2+} vacancies in HAPNs were assumed to be uniformly distributed, and the dielectric constants ε' and ε'' were considered close to those of imperfect HAP crystals [42] and water [17], approximately 15 and 80, respectively. These values do not account for: (i) substantial distance-dependent variations in ε'' near the HAPN surface [43], (ii) interface morphology, (iii) acceleration of molecular motion in external potentials [44,45], and (iv) the dependence of ε' on specific imperfections in bioapatite. Besides, the condition $L >> \frac{d}{2}$ assumed by Equations (4) and (5), requires further investigations as applied to nanoelements. The finite spatial extent of the charge distribution on the negative and positive plates was also ignored.

Since the contribution of PO_4^{3-} ions to Q_{surf} was not considered, both the potential difference and electrostatic field strength may be underestimated. Therefore, the actual electrostatic fields may be stronger than the values estimated in the present work.

The inferred polarization and ordering of PO_4^{3-} ions at the interface are notable because the prevailing view assumes significant structural disorder in this region (see, e.g., [21]). Although this does not imply restoration of crystalline order, it suggests that the interfacial region may not be fully comparable to amorphous calcium phosphate [46].

To clarify this feature, Raman signals from bone tissue can be compared with those from invertebrate exoskeletons. Raman spectra of the exoskeleton enable effective probing of CO_3^{2-} ions in different chemical environments [47] as $CaCO_3$ polymorphs form the mineral phase of invertebrates. The studies of the $\nu_1[CO_3^{2-}]$-band shapes face similar difficulties in understanding their asymmetry compared to the band in the reference spectra of calcium carbonates. According to Wehrmeister et al. [47], the $\nu_1[CO_3^{2-}]$-band is composed of two components: the high-frequency Lorentzian at 1088 cm^{-1} and the low-frequency Gaussian at 1078 cm^{-1}. These components correspond, respectively, to nanocrystalline $CaCO_3$ and amorphous calcium carbonate phases. In particular, these compositions have been identified in the palm region of the claw of Callinectes sapidus and in the exoskeleton of Calappa granulata [48,49].

Examining the Raman $\nu_1[CO_3^{2-}]$ band in combination with Ca 2p NEXAFS spectroscopy and electron microscopy data, Katsikini and co-authors [48] confirmed the assignment of Lorentzian and Gaussian sub-bands to crystalline and amorphous $CaCO_3$ phases, respectively, and linked their intensities to site-dependent variations in exoskeleton crystallinity.

At first glance, the two-component structure of the $\nu_1[PO_4^{3-}]$ and $\nu_1[CO_3^{2-}]$ bands appear to indicate a similar origin. However, the different distributions of Gaussian and Lorentzian components suggest different underlying origins for these bands. To investigate this difference, it can be assumed that the $\nu_1[PO_4^{3-}]$ band may also have a mixed crystalline–amorphous origin. This assumption is supported by Raman studies of amorphous calcium phosphates [50,51], in which the $\nu_1[PO_4^{3-}]$ band is observed at 10–13 cm^{-1} lower than in crystalline HAP, corresponding to the same Raman shift region as sub-band *B*.

To evaluate the proposed crystalline–amorphous origin of the $\nu_1[PO_4^{3-}]$ band asymmetry, Lorentzian and

Gaussian profiles were assigned to the high- and low-frequency components, respectively. However, the resulting fit quality, with $\chi^2 \approx 1817$, was nearly eightfold poorer than that obtained for the fitting presented in Figure 3. This poorer fit does not necessarily exclude a contribution from mixed crystalline and amorphous phases to the $v_1(PO_4^{3-})$ band in bone; however, it indicates that other dominant mechanisms may govern its spectral features. One possible interpretation is dipole polarization of PO_4^{3-} ions and their ordering within intrinsic electrostatic fields in bone. Accordingly, the results do not support the interpretation that the low-frequency shoulder arises mainly from amorphous mineral; rather, they are more consistent with ordered but distorted PO_4^{3-} groups at the interface under strong electric fields.

Despite the small magnitude of the displacement Δ_A reported in Section 3.3, its direction is important because it supports the proposed influence of electrostatic fields on atomic dynamics. This direction cannot be explained by adiabatic compression of PO_4^{3-} ions, because the HAP unit cell is less compressed in young bone than in mature bone [28]. In that case, an upward shift would be expected. Therefore, the observed behavior may instead be attributed to electrostatic interactions, particularly Coulomb repulsion between anions within HAPNs. As $|Q(\text{mature})| < |Q(\text{young})|$, the frequency ω of P-O stretching decreases with age, resulting in $E_A(\text{young}) > E_A(\text{mature})$. This behavior may serve as an indicator of age-related dissipation of charge Q.

The weakening of electrostatic fields and the growth of HAPNs with age are qualitatively consistent with inequality (7). However, the observed decrease in the relative intensity $\frac{B}{A+B}$ is smaller than expected based on the extracted changes in charge and size (see Table 2). This discrepancy may be associated with preservation of dipole orientation during the deposition of additional atomic layers as HAPNs grow, suggesting a possible memory effect in dipole orientation during bone aging.

Further confirmation of the memory effect can be obtained by analyzing the cumulative changes in the Lorentzian and Gaussian contributions to the $v_1[PO_4^{3-}]$-band with age. The coefficient $\frac{L}{G}$ was introduced as follows:

$$\frac{L}{G} = \frac{W_A^L \frac{A}{A+B} + W_B^L \frac{B}{A+B}}{W_B^G \frac{A}{A+B} + W_B^G \frac{B}{A+B}}. \quad (8)$$

This coefficient represents the relative Lorentzian-to-Gaussian contribution to the overall band shape. The $\frac{L}{G}$ coefficients computed for young bone, mature bone, and the HAP crystal using Equation (8) and experimental data are given in Table 2. The Lorentzian contribution is lowest in young bone; although static disorder decreases with age, the $\frac{L}{G}$ coefficient increases and, in mature bone, approaches the value characteristic of the HAP crystal. This result further confirms the applicability of the chosen method of $v_1[PO_4]^{3-}$ bandshape analysis using Voigt functions.

4.2. Prospects

The assessment of electrostatic fields in mineralized bone suggests: (i) an important role of these fields at HAPN interfaces and (ii) a substantial reduction in their strength with age. It should be noted that the decrease is quite dramatic, because the expected potential difference $\Delta\varphi$ for young bone noticeably exceeds the kinetic energy (k_BT) of the thermal motion of atoms, whereas in mature bone the difference $\Delta\varphi$ is virtually smoothed out by the thermal movements. It is also noted that $\Delta\varphi$ in young bone exceeds the membrane potential (70–90 mV), but is substantially lower in mature bone.

The predicted variations in the potential $\varphi(r)$ suggest the possibility of quantum effects such as electron trapping in potential wells and electron tunneling through potential barriers (see Figure 5) as charge carriers propagate through bone mineral. To quantify the valence band structure of bone, a three-dimensional superlattice model was previously proposed [52]. The model relates the valence band energy in bone to the electron-optical properties of the supercell S using the relation

$$e^{2ikb_j} - 2Re\left(\frac{1}{T(E)}\right)e^{ikb_j} + 1 = 0. \quad (9)$$

This relation links the electron energy E to the wave vector k in the super periodic potential of a conglomerate, where T denotes the electron transmission amplitude through supercell S and bj represents the mean dimension of S in the j-direction. In solid-state physics, this relation is known as the Heine equation [53].

The three-dimensional superlattice model predicts the red shift $\Delta_n = E_n^{\text{HAP}} - E_n^{\text{bone}} \approx 2E_n \frac{<\tilde{d}>}{<L>} > 0$ of valence bands in bone mineral compared to those, E_n^{HAP}, in HAP crystal, and links the shift with super-long-order parameters of conglomerate and with peculiarities of electrons propagation through the conglomerate. $<\tilde{d}>$ and $<L>$ are respectively the electron-optical length of hydrated nanolayers and the mean linear size of HAPN. As the potential $\varphi(r)$ is found to vary substantially with age, an essential age dependence of the electron-optical length $<\tilde{d}>$ can be predicted. Therefore, the valence band en-

2026, Vol. 3, Article ID. 2026.0028
https://doi.org/10.69709/BIOMATC.2026.166607

ergy E_n^{bone} in mineralized bone may be an age-dependent characteristic of its electronic structure.

X-ray dichroism observed in photoemission from cortical bone [54] also suggests that charge transfer and related quantum phenomena may depend on the orientation of HAPNs relative to the principal axes of bone. According to the Wolff paradigm [55], bone structural orientation is governed by locomotor function and mechanical loading against gravity. It may therefore be hypothesized that the quantization axes of bone nanostructures are related to the directions of gravitational forces within the skeleton. This suggests that studies of biomineralization mechanisms may need to consider quantum effects in relation to gravitational orientation. Accordingly, quantum phenomena may play a role in bone tissue, particularly in the propagation of molecular signals along its structure [56]. These phenomena warrant further detailed investigation and are therefore not discussed further here.

The built-in charge Q and the energy $\mathcal{E}$ are determined not only by Ca^{2+} vacancies, calcium deficiency, and geometry of HAPN, but also by substitutions at all crystallographic positions, which affect the charge. Thus, for example, substitution of Ca^{2+} by Na^{+} and OH^{-} by O^{2-} increases Q, whereas carbonation decreases it. The effects of such substitutions, which may be influenced by environmental and nutritional factors, were not considered in the present study. Further research is required to evaluate their impact on the electrophysical properties of bone and to enable more rigorous quantitative validation of the BB concept.

5. Conclusions

This study shows that electrostatic fields generated by built-in charges in HAPNs can significantly influence the atomic structure and dynamics of native bone. In young bone, a potential difference $\Delta\varphi$ between negatively charged bioapatite nanocrystal surfaces and positively charged hydrated nanolayers is expected to be maximal. In mature bone, both the potential difference $\Delta\varphi$ and the electric field strength F are reduced by approximately one order of magnitude.

The experimental analysis revealed a two-component structure of the $v_1(PO_4^{3-})$ band, which may reflect different effects of electrostatic fields in the bulk and at the interfaces of HAPNs. The bulk component exhibits a predominantly Gaussian profile, whereas the interfacial component displays a distinct Lorentzian character. This difference is attributed to polarization and ordering of phosphate ions at the interface, induced by internal electric fields in bone. This interdisciplinary study confirms the BB concept and reveals the important role of internal electrostatic fields in mineralized bone. In young bone, the potential difference between the negatively charged HAPN surfaces and the positively charged hydrated nanolayers is estimated to be 140 ± 50 mV. In mature bone, this difference decreases approximately 10-fold. Consistent with this estimate, experimental analysis of the Raman spectra reveals a specific age-dependent two-component structure of the v1[PO4]3- -band, which reflects changes in P - O stretching caused by variations in electric field strengths in the bulk and at the HAPN interface. The bulk component exhibits a predominantly Gaussian shape, while the interface component has a distinct Lorentzian shape. This specific shaping is explained by the significant dipole polarization and ordering of phosphate ions at the interfaces.

It has been speculated that early-formed dipoles may retain their orientation during later growth, which could explain the observed trend, and predict the specific quantization of electronic states in the mineral matrix and the alignment of the quantization axes along the directions of gravitational forces the skeleton.

Overall, this work may contribute to the design of bioinspired energy materials, the development of targeted drug delivery strategies based on bone charge properties, and the advancement of electrophysical approaches for bone health monitoring.

List of Abbreviations

BB	Bone Battery
BE	Binding Energy
DEL	Double Electric Layer
HAP	Hydroxyapatite
HAPN	Hydroxyapatite Nanocrystal
ISO	International Organization for Standardization
NMR	Nuclear Magnetic Resonance
XPS	X-ray Photoelectron Spectroscopy
XRD	X-ray Diffraction

Author Contributions

Conceptualization: A.P.; Methodology: A.P., X.B., Al.K., A.C., and An.K.; Software: X.B. and Al.K.; Validation: A.P., Al.K., and An.K.; Formal analysis: A.P., X.B., Al.K., A.C., and An.K.; Investigation: Al.K. and A.C.; Resources: X.B., Al.K., A.C., and An.K.; Data curation: X.B., Al.K., A.C., and An.K.; Writing—original draft: A.P., Al.K., and A.C.; Visualization: A.P. and X.B.; Supervision: A.P.; Funding acquisition: A.P. All co-authors contributed to the discussion of the results and have read and agreed to the published version of the manuscript.

Availability of Data and Materials

The data are available upon contacting the resource centers of the Science Park of St. Petersburg State University (https://docs.researchims.ru/common/registration/).

Ethics Committee Approval

The study protocol (No. 10-10-2015) was approved after review by the Local Ethic Committee of R.R. Vreden National Medical Research Center of Traumatology and Orthopedics.

Animals Rights Statement

All experimental procedures involving animals were performed in accordance with the ARRIVE guidelines. The study complied with all applicable national laws, regulations, and guidelines, including GOST R ISO 10993-2-2009 (Medical devices—Biological evaluation of medical devices; Part 2: Animal welfare requirements), which ensures high standards of animal welfare, as well as GOST 33215-2014 and GOST 33216-2014, which specify the rules for the maintenance and care of laboratory rodents and rabbits. All animals were housed under identical conditions in the vivarium of the National Medical Research Center of Traumatology and Orthopedics.

Conflicts of Interest

The authors declare no conflicts of interest.

Funding

This work is financially supported by the Russian Science Foundation Grant 23-21-00172.

Acknowledgments

This research was carried out with the technical support of the Center for Physical Methods of Surface Investigation, Center for Diagnostics of Functional Materials for Medicine, Pharmacology and Nanoelectronics and Center for Optical and Laser Methods for Studying Matter at St. Petersburg State University.

AI Declaration

The authors confirm that no AI tools were used to generate any content of this manuscript.

References

[1] Guo, J.; Gao, F.; Zhang, F.; Zhao, X.; Zhao, R. Biomineralization-Driven Advances in Materials Science and Biomedical Engineering. *JACS Au* **2025**, *5*, 4134–4154. [CrossRef]

[2] Gilbert, P.U.P.A.; Bergmann, K.D.; Boekelheide, N.; Tambutté, S.; Mass, T.; Marin, F.; Adkins, J.F.; Erez, J.; Gilbert, B.; Knutson, V.; et al. Biomineralization: Integrating Mechanism and Evolutionary History. *Sci. Adv.* **2022**, *8*, eabl9653. [CrossRef]

[3] Yan, X.; Zhang, Q.; Ma, X.; Zhong, Y.; Tang, H.; Mai, S. The Mechanism of Biomineralization: Progress in Mineralization from Intracellular Generation to Extracellular Deposition. *Jpn. Dent. Sci. Rev.* **2023**, *59*, 181–190. [CrossRef] [PubMed]

[4] Vernadsky, V.I. *Biosphere*; Scientific Chemical Technical Publishing House, Scientific and Technical Department: Leningrad, Russia, 1926; 146p. Available online: https://cat.gpntb.ru/?id=FT/ShowFT&sid=4c1c7cd819e2ca204bb346e7cb8f9880.

[5] Barinov, S.M. Calcium Phosphate-Based Ceramic and Composite Materials for Medicine. *Russ. Chem. Rev.* **2010**, *79*, 13–29. [CrossRef]

[6] Samoylov, Y.B. *Biolytes*; Scientific Chemical Technical Publishing House: Leningrad, Russia, 1929; 140p. Available online: https://www.lvb.lt/discovery/fulldisplay/alma9910096364708451/.

[7] Iafisco, M.; Delgado-López, J.M. (Eds.) *Apatite: Synthesis, Structural Characterization and Biomedical Applications in Geology and Mineralogy Research Developments Materials Science and Technologies Series/Geology and Mineralogy Research Developments*; Nova Science Publishers: Hauppauge, NY, USA, 2014; 364p, ISBN 978-1-63321-536-8. Available online: https://www.researchgate.net/publication/265614312_Apatite_Synthesis_Structural_Characterization_and_Biomedical_Applications.

[8] Landis, W.J.; Hodgens, K.J.; Arena, J.; Song, M.J.; McEwen, B.F. Structural Relations Between Collagen and Mineral in Bone as Determined by High Voltage Electron Microscopic Tomography. *Microsc. Res. Tech.* **1996**, *33*, 192–202. [CrossRef]

[9] Lin, K.; Wu, C.; Chang, J. Advances in Synthesis of Calcium Phosphate Crystals with Controlled Size and Shape. *J. Acta Biomater.* **2014**, *10*, 4071–4102. [CrossRef]

[10] Denisov-Nikolski, Y.I.; Mironov, S.P.; Omeljanenko, N.P.; Omelianenko, I.V. *Actual Problems of Theoretical and Clinical Osteoartrology*; M. JSC Printing-House "News": Moscow, Russia, 2005; 336p. Available online: https://scholar.google.com/scholar?q=Denisov-Nikolski+Mironov+Omeljanenko+Actual+Problems+of+Theoretical+and+Clinical+Osteoartrology+2005.

[11] Avrunin, A.S.; Tikhilov, R.M.; Abolin, A.B.; Shcherback, I.G. Levels of bone mineral matrix organization and the mechanisms determining parameters of its formation. *Morphology* **2005**, *2*, 78–82. (In Russian) [View Online]

[12] Yao, S.; Jin, B.; Liu, Z.; Shao, C.; Zhao, R.; Wang, X.; Tang, R. Biomineralization: From Material Tactics to Biological Strategy. *Adv. Mater.* **2017**, *29*, 1605903. [CrossRef] [PubMed]

[13] Cuéllar-Cruz, M. Synthesis of Inorganic and Organic Crystals Mediated by Proteins in Different Biological Organisms. A Mechanism of Biomineralization Conserved Throughout Evolution in All Living Species. *Prog. Cryst. Growth Charact. Mater.* **2017**, *63*, 94–103. [CrossRef]

[14] Engel, J. *A Critical Survey of Biomineralization. Control, Mechanisms, Functions and Material Properties*; Springer Briefs in Applied Sciences and Technology; Springer International Publishing: Cham, Switzerland, 2017; 64p. [CrossRef]

[15] Deymier, A.C.; Nair, A.K.; Depalle, B.; Qin, Z.; Arcot, K.; Drouet, C.; Yoder, C.H.; Buehler, M.J.; Thomopoulos, S.; Genin, G.; et al. Protein-Free Formation of Bone-Like Apatite: New Insights into the Key Role of Carbonation. *Biomaterials* **2017**, *127*, 75–88. [CrossRef]

[16] Lotsari, A.; Rajasekharan, A.K.; Halvarsson, M.; Andersson, M. Transformation of Amorphous Calcium Phosphate to Bone-Like Apatite. *Nat. Commun.* **2018**, *9*, 4170. [CrossRef] [PubMed]

[17] Brykalova, X.O.; Kornilov, N.N.; Pavlychev, A.A. The Peculiarities of Charge Distribution and Spatiotemporal Changes in Electronic and Atomic Structure of Bone Tissue. *J. Mater. Chem. A* **2022**, *10*, 22686–22693. [CrossRef]

[18] Wopenka, B.; Pasteris, J.D. A Mineralogical Perspective on the Apatite in Bone. *Mater. Sci. Eng. C* **2005**, *25*, 131–143. [CrossRef]

[19] Sun, Y.; Wang, Y.; Ji, C.; Ma, J.; He, B. The Impact of Hydroxyapatite Crystal Structures and Protein Interactions on Bone's Mechanical Properties. *Sci. Rep.* **2024**, *14*, 9786. [CrossRef]

[20] Pavlychev, A.A.; Brykalova, X.O.; Cherny, A.A.; Korneev, A.V.; Kornilov, N.N. Spatiotemporal Changes in Atomic and Molecular Architecture of Mineralized Bone under Pathogenic Conditions. *Crystals* **2023**, *13*, 381. [CrossRef]

[21] Avrunin, A.S.; Pavlychev, A.A.; Doctorov, A.A.; Vinogradov, A.S.; Samoilenko, D.O.; Svirsky, G.I. Influence of the Skeleton Hierarchical Organization on Electronic State of Ions in Bone Matrix. *Traumatol. Orthop.* **2016**, *22*, 88–97. [CrossRef]

[22] Frank-Kamenetskaya, O.; Kol'tsov, A.; Kuz'mina, M.; Zorina, M.; Poritskaya, L. Ion Substitutions and Non-Stoichiometry of Carbonated Apatite-(CaOH) Synthesised by Precipitation and Hydrothermal Methods. *J. Mol. Struct.* **2011**, *992*, 9–18. [CrossRef]

[23] Xu, Y.; Galloway, J.M.; Hasselt, L.J.; Meldrum, F.C. The Role of Confinement in Biomineralization Meldrum. *Chem. Rev.* **2025**, *125*, 12128–12197. [CrossRef]

[24] Mandair, G.S.; Morris, M.D. Contributions of Raman Spectroscopy to the Understanding of Bone Strength. *BoneKey Rep.* **2015**, *4*, 620. [CrossRef] [PubMed]

[25] Penel, G.; Delfosse, C.; Descamps, M.; Leroy, G. Composition of Bone and Apatitic Biomaterials as Revealed by Intravital Raman Microspectroscopy. *Bone* **2005**, *36*, 893–901. [CrossRef] [PubMed]

[26] Gouadec, G.; Colomban, P. Raman Spectroscopy of Nanomaterials: How Spectra Relate to Disorder, Particle Size and Mechanical Properties. *Prog. Cryst. Growth Charact. Mater.* **2007**, *53*, 1–56. [CrossRef]

[27] Pavlychev, A.A.; Brykalova, X.O.; Korneev, A.V.; Cherny, A.A.; Kornilov, N.N. Specific Features of the Crystal Structure of Calcium Hydroxyapatite in Native Bone Tissue. *Crystallogr. Rep.* **2024**, *69*, 38–44. [CrossRef]

[28] Frank-Kamenetskaya, O.V.; Vlasov, D.Y.; Panova, E.G.; Lessovaia, S.N. (Eds.) *Processes and Phenomena on the Boundary Between Biogenic and Abiogenic Nature*; Lecture Notes in Earth System Sciences (Book Series); Springer: Cham, Switzerland, 2020. [CrossRef]

[29] Colomban, P.; Sagon, G.; Faurel, X. Differentiation of Antique Ceramics from the Raman Spectra of their Colored Glazes and Paintings. *J. Raman Spectrosc.* **2001**, *32*, 351. [CrossRef]

[30] Gouadec, G.; Colomban, P.; Bansal, N.P. Raman Study of Hi-Nicalon Fiber Reinforced Celsian Composites, Part1: Distribution and Nanostructure of Different Phases. *J. Am. Ceram. Soc.* **2001**, *84*, 1129. [CrossRef]

[31] Colomban, P.; Gouadec, G.; Mazerolles, L. Raman Analysis of Materials Corrosion: The Example of SiC Fibers. *Mater. Corros.* **2002**, *53*, 306. [CrossRef]

[32] Cabot, A.; Diéguez, A.; Romano-Rodriguez, A.; Morante, J.R.; Barsan, N. Influence of the Catalytic Introduction Procedure on the Nano-SnO_2 Gas Sensor Performances. Where and How Stay the Catalytic Atoms? *Sens. Actuators B* **2001**, *79*, 98. [CrossRef]

[33] Cassoux, P.; de-Caro, D.; Valade, L.; Casellas, H.; Roques, S.; Legros, J.-P. Thin Films and Nanowires of Molecule-Based Conductors and Magnets. *Synth. Met.* **2003**, *133–134*, 659. [CrossRef]

[34] Fang, G.J.; Yao, K.-L.; Liu, Z.-L. Fabrication and Electrochromic Properties of Double Layer WO3(V)/V2O5(Ti) Thin Films Prepared by Pulsed Laser Ablation Technique. *Thin Solid Film.* **2001**, *394*, 64. [CrossRef]

[35] Poborchii, V.V. Raman Spectra of Sulfur, Selenium or Tellurium Clusters Confined in Nano-Cavities of Zeolite A. *Solid State Comm.* **1998**, *107*, 513. [CrossRef]

[36] Rodríguez-Cabello, J.C.; Quintanilla, L.; Pastor, J.M. Fourier Transform Raman Study of the Conformers in Poly(Ethylene Terephtalate). *J. Raman Spectrosc.* **1994**, *25*, 335. [CrossRef]

[37] Li, X.; Chen, W.; Bian, C.; He, J.; Xu, N.; Xue, G. Surface Modification of TiO_2 Nano Particles by Polyaniline. *Appl. Surf. Sci.* **2003**, *217*, 16. [CrossRef]

[38] Pavlychev, A.; Brykalova, X.; Cherny, A.; Konashuk, A.; Korneev, A. *Mechanical Loads and Site-Dependent Changes in Crystal Structure and Molecular Dynamics in Native Bone*; Springer Series Book Machine and Materials Science Vol. 156, Chapter 33;

Yue, X., Yuan, K., Eds.; Springer: Berlin/Heidelberg, Germany, 2023. [CrossRef]

[39] Aggarwal, R.L.; Farrar, L.W.; Greeneltch, N.G.; Van Duyne, R.P.; Polla, D.L. Measurement of the Raman Line Widths of Neat Benzenethiol and a Self-Assembled Monolayer (SAM) of Benzenethiol on a Silver-Coated Surface-Enhanced Raman Scattering (SERS) Substrate. *Appl. Spectrosc.* **2012**, *66*, 740–743. [CrossRef] [PubMed]

[40] Tu, Z.; Achazi, K.; Schulz, A.; Mülhaupt, R.; Thierbach, S.; Rühl, E.; Adeli, M.; Haag, R. Combination of Surface Charge and Size Controls the Cellular Uptake of Functionalized Graphene Sheets. *Adv. Funct. Mater.* **2017**, *27*, 1701837. [CrossRef]

[41] Wilson, E.E.; Awonusi, A.; Morris, M.D.; Kohn, D.H.; Tecklenburg, M.M.; Beck, L.W. Highly Ordered Interstitial Water Observed in Bone by Nuclear Magnetic Resonance. *J. Bone Min. Res.* **2005**, *20*, 625–634. [CrossRef]

[42] Zakharov, N.A.; Orlovsky, V.P. Dielectric Characteristics of Biocompatible $Ca_{10}(PO_4)_6(OH)_2$ Ceramics. *Tech. Phys. Lett.* **2001**, *27*, 629–631. [CrossRef]

[43] Qi, C.; Zhu, Z.; Wang, C.; Zheng, Y. Anomalously Low Dielectric Constant of Ordered Interfacial Water. *J. Phys. Chem. Lett.* **2021**, *12*, 931–937. [CrossRef]

[44] Olivieri, F.; Hynes, J.T.; Laage, D. Confined Water's Dielectric Constant Reduction Is Due to the Surrounding Low Dielectric Media and Not to Interfacial Molecular Ordering. *J. Phys. Chem. Lett.* **2021**, *12*, 4319–4326. [CrossRef]

[45] Zhang, Y.; de Aguiar, H.B.; Hynes, J.T.; Laage, D. Water Structure, Dynamics, and Sum-Frequency Generation Spectra at Electrified Graphene Interfaces. *J. Phys. Chem. Lett.* **2020**, *11*, 624–631. [CrossRef] [PubMed]

[46] Dorozhkin, S.V. Amorphous Calcium Orthophosphates: Nature, Chemistry and Biomedical Applications. *Int. J. Mater. Chem.* **2012**, *2*, 19–46. [CrossRef]

[47] Wehrmeister, U.; Jacob DESoldati, A.L.; Loges, N.; Häger, T.; Hofmeister, W. Amorphous, Nanocrystalline and Crystalline Calcium Carbonates in Biological Materials. *J. Raman Spectrosc.* **2010**, *42*, 926–935. [CrossRef]

[48] Katsikini, M.; Proiou, E.; Vouroutzis, N.; Pinakidou, F.; Paloura, E.C.; Smirnov, D.; Brzhezinskaya, M.; Ves, S. Crystalline and Amorphous Calcium Carbonate as Structural Components of the *Calappa granulata* Exoskeleton. *J. Struct. Biol.* **2020**, *211*, 107557. [CrossRef] [PubMed]

[49] Jacob, D.E.; Wirth, R.; Soldati, A.L.; Wehrmeister, U.; Schreiber, A. Amorphous Calcium Carbonate in the Shells of Adult Unionoida. *J. Struct. Biol.* **2011**, *173*, 241–249. [CrossRef]

[50] Combes, C.; Rey, C. Amorphous Calcium Phosphates: Synthesis, Properties and Uses in Biomaterials. *Acta Biomater.* **2010**, *6*, 3362–3378. [CrossRef]

[51] Demnati, I.; Grossin, D.; Marsan, O.; Bertrand, G.; Collonges, G.; Combes, C.; Parco, M.; Braceras, I.; Alexis, J.; Balcaen, Y.; et al. Comparison of Physical-Chemical and Mechanical Properties of Chlorapatite and Hydroxyapatite Plasma Sprayed Coatings. *Open Biomed. Engin. J.* **2015**, *9*, 42–55. [CrossRef] [PubMed]

[52] Pavlychev, A.A.; Avrunin, A.S.; Vinogradov, A.S.; Filatova, E.O.; Doctorov, A.A.; Krivosenko, Y.S.; Samoilenko, D.O.; Svirskiy, G.I.; Konashuk, A.S.; Rostov, D.A. Local Electronic Structure and Nanolevel Hierarchical Organization of Bone Tissue: Theory and NEXAFS Study. *Nanotech* **2016**, *27*, 504002. [CrossRef]

[53] Cohen, M.L.; Heine, V. The Fitting of Pseudopotentials to Experimental Data and Their Subsequent Application. *Solid State Phys.* **1970**, *24*, 37–248. [CrossRef]

[54] Konashuk, A.S.; Brykalova, X.O.; Kornilov, N.N.; Filatova, E.O.; Pavlychev, A.A. Hierarchy-Induced X-Ray Linear Dichroism in Cortical Bone. *Emerg. Mater.* **2020**, *3*, 515–520. [CrossRef]

[55] Wolff, J. *Das Gesetz der Transformation der Knochen*; Hirschwald: Berlin, Germany, 1892. [CrossRef]

[56] Shah, H.N.; Amanatullah, D.F.; Longaker, M.T.; Lowenberg, D.W. Bridging Technique and Science: A Review of the Molecular Signals from Long Bone Development That Guiding Bone Regeneration. *Orthoplastic Surg.* **2022**, *9*, 86–92. [CrossRef]